IEEE Access
Multidisciplinary | Rapid Review | Open Access Journal

SPECIAL SECTION ON GNSS, LOCALIZATION, AND NAVIGATION TECHNOLOGIES

Received December 1, 2017, accepted January 8, 2018, date of publication January 17, 2018, date of current version March 16, 2018.

Digital Object Identifier 10.1109/ACCESS.2018.2794524

A Bionic Polarization Navigation Sensor Based on Polarizing Beam Splitter

JIAN YANG[1], TAO DU[2], BEN NIU[3], CHENYANG LI[3], JIANQIANG QIAN[4], AND LEI GUO[3], (Senior Member, IEEE)

[1]School of Instrumentation Science and Opto-electronics Engineering, Beihang University, Beijing 100191, China
[2]School of Electronics and Information Engineering, North China University of Technology, Beijing 100144, China
[3]School of Automation Science and Electrical Engineering, Beihang University, Beijing 100191, China
[4]School of Physics and Nuclear Energy Engineering, Beihang University, Beijing 100191, China

Corresponding author: Lei Guo (lguo@buaa.edu.cn)

This work was supported by the National Natural Science Foundation of China under Grant 61627810, Grant 61320106010, Grant 61703006, Grant 61661136007, and Grant 61573019.

ABSTRACT Polarization navigation has been an active research direction in navigation fields due to its autonomy and robustness, especially in global navigation satellite system-denied environment. Most existing bionic polarization sensing schemes employed the linear polarizer as the analyzer. However, the quadrature error between the two sets of mutually orthogonal polarizers is usually inevitable, which may cause the sensor output distortion and directly affect the performance of polarization navigation sensors. In this paper, inspired by the special polarization-sensitive structure of insect compound eyes, a polarizing beam splitter (PBS) based polarization navigation sensor is designed. Concerned with the optical path coupling and extinction ratio inconsistency problem between the transmitted beam and the reflected one of the PBS, the novel sensor model is established, where we introduce a coupling coefficient to solve the problems mentioned above. An algorithm of computing the polarization degree and the polarization azimuth angle is presented based on the model. The unscented Kalman filter calibration method is adopted and the calibration experiments are carried out. Finally, the outdoor static accuracy of the sensor is tested, where the results showed that the sensor designed in this paper achieved high accuracy and good stability for a long time.

INDEX TERMS Quadrature error, polarization beam splitter, sensor model, coupling coefficient, calibration, high accuracy.

I. INTRODUCTION

It has been widely observed that that many kinds of creatures are born with the instinct to navigate themselves according to the earth's magnetic field, the position of the Sun, the landmarks or the polarized skylight [1]–[3]. The pattern of the polarization is a very robust pattern, which can be described as the direction of polarization and degree of polarization [4], [5]. Many creatures use the stable distribution pattern as a compass to determine the direction towards their home [6], [7]. In the past decades, the existence of polarization vision has been found in a variety of organisms, which attracted significant research efforts on bionic polarization navigation systems from the perspectives of multi-disciplinary research in both biological sciences and engineering technologies [8].

The polarization navigation has the advantages of being highly autonomous, robust and anti-disturbance [9], [10], to name just a few. It has been one of the central research topics in the field of autonomous navigation, with a wide range of applications, especially when GNSS signal is fragile to nature or human jams [11]–[13]. Therefore, the investigation on the bionic polarization sensor has been particularly important in the biomimetic field nowadays.

Inspired by animals' navigation capability, scholars have designed various bionic polarization navigation sensors with structures similarly to those of biological compound eyes. For example, by imitating the navigation strategy of desert ants, Cataglyphis, Lambrinos *et al.* [14], [15] adopted a polarization-sensitive compass to assist the Sahabot robot navigation system, and realized autonomous navigation. Combined with polarization compass, panoramic visual system and ambient-light sensors, they demonstrated the navigation capabilities similar to insects. In 2008, Chu *et al.* [16] constructed a six-channel navigation sensor and tested the

sensor accuracy under various outdoor skylight conditions. Subsequently, they proposed a polarization azimuth angle algorithm to achieve a higher accuracy with consistent input errors and effectively overcome the overflow problem of division by zero [17]. Luo *et al.* [18] reported a polarization sensor with photoelectric and proposed a polarization azimuth calculation method. In their results, the range of polarization azimuth angle was predetermined and the right channels were chosen reasonably. In 2015, Ma *et al.* [19] designed a polarization navigation sensor containing six POL-sensors and presented a new calibration model which take advantage of both of reference angle of polarization and constant degree of polarization. They calibrated the sensor by using the NSGA-II algorithm and the experiment results show that the proposed algorithm is more stable than the LS method [20]. By using the spectral, spatial and polarized skylight, Chahl and Mizutani [4] developed a polarization compass and multispectral panoramic image device for navigation and stabilization. With various static and flight tests, their results indicated that the biomimetic sensors can achieve the same level of accuracy as that of the solid state magnetic compass.

Recent publications in this field reported some representative new techniques and approaches, including nanotechnology and polarization vision. For example, Zhang *et al.* [21] innovatively integrated six single-layer nanowire gratings into a polarization sensitive structure, with the precision of the sensor $< \pm 0.1^\circ$ in indoor tests. Further result in this field is also presented by Wang *et al.* [22], where a polarization navigation sensor is integrated by single-layer nanowire polarizers with photo detectors, which demonstrates the measurement error of less than $\pm 1.5^\circ$ in the outdoor test. In the research field of polarization vision, Sarkar *et al.* [23] and [24] presented a polarization navigation system based on a CMOS image sensor by using a metallic wire grid micro-polarizer for the first time. They employed this methodology to measure the polarization information of the observation area in real time. The proposed CMOS polarization sensor is only occupying an area of 5 mm $\times$ 4 mm, but the accuracy of the sensor is improved significantly. Meanwhile, a camera-based polarization sensor is designed by Fan *et al.* [25] and later, Wang *et al.* [26], where the polarization orientation algorithms were proposed by establishment of the sun vector and the estimate of the solar meridian, achieved the resulting standard deviations of 0.28°.

In the above-mentioned results, polarizers have been widely used as the analyzer. However, the quadrature error between the two sets of mutually orthogonal polarizers is one of the error sources of the sensor, which may cause non-sinusoidal distortion to the sensor output, detailed seen in Section II. In this paper, to eliminate the quadrature error on sensor accuracy and stability, we designed a bionic polarization navigation sensor based on polarizing beam splitter (PBS). The PBS can divide a beam of incident natural light into two mutually perpendicular beams of polarized light. This design is biomimetic and can better simulate the polarization-sensitive photoreceptor cells of insect compound eyes [7], [27]. Furthermore, by using the PBS, the sensor is highly integrated, which is convenient for unmanned aerial vehicle (UAV) applications.

The main contribution of this work is highlighted as follows:

1) inspired by the polarization-opponent (POL-OP) unit of insect compound eyes, a new structure of polarization sensor is designed based on polarizing beam splitter (PBS). By using PBS as the sensor analyzer, the quadrature error between the two sets of mutually orthogonal polarizers is eliminated;
2) different from the existing sensor models, we introduced a coupling coefficient to solve the problem of optical coupling and extinction ratio inconsistency of PBS.

Accordingly, the remainder of this paper is organized as follows. In Section II, the new structure and the hardware design of the sensor are briefly described. In Section III, we improve the existing sensor model by introducing a coupling coefficient that characterizes the polarization degree, which can better deal with the coupling and extinction ratio inconsistency problems between the transmitted polarized light and the reflected one of the PBS. Then, a polarization calculation algorithm based on independent channel is presented, where the UKF method is also adopted to calibrate and identify the sensor parameters in Section IV. Finally, indoor calibration and outdoor static accuracy experiments are carried out to verify the sensor performance in Section V.

II. SENSOR DESIGN

It is well known that the polarized skylight is sensed by highly aligned polarization-opponent (POL-OP) units in dorsal rim area (DRA) of insects ommatidium [27]. In each POL-OP unit, there are two photoreceptor channels with the directions of polarization are perpendicular to each other, as shown in Fig.1(a). According to this special polarization-sensitive structure, various of polarization sensors have been designed by scholars. Most existing sensors consisting of three groups of POL-OP units and the linear polarizer is used as the analyzer of the polarization sensor, the general polarizer installation schematic diagram can be seen in Fig.1 (b). Each unit has two channels, wherein the polarization directions between channel-1 and channel-2 are mutually orthogonal.

However, by using the polarizer as sensor analyzer will bring quadrature error, which will result in non-sinusoidal distortion of sensor output. Taking Group A as an example, the polarizer polarization directions of channel-1 and channel-2 are set to 0° and 90°, respectively. In practice, it is difficult to ensure the directions of polarization between the two polarizers are strictly perpendicular to each other. In the laboratory standard light environment, we placed the polarizer based sensor on a high-precision turntable, and the turntable turned 360° and collected 360 samples in total. Fig. 2 shows that there is a phase delay between channel-1 and channel-2.

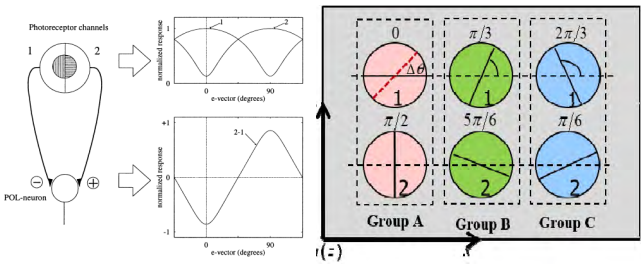

FIGURE 1. Polarization-opponent unit and the polarizer installation diagram. (a) The polarization-opponent units consist of two mutually orthogonal photoreceptor channels (1 vs. 2) [15]. By the POL neurons, insects convert the polarization optical signal into electrical signal which is used to heading orientation. (b) Three groups of polarization-opponent unit installation directions, there exists a quadrature error $\Delta\theta$ between channel-1 and channel-2.

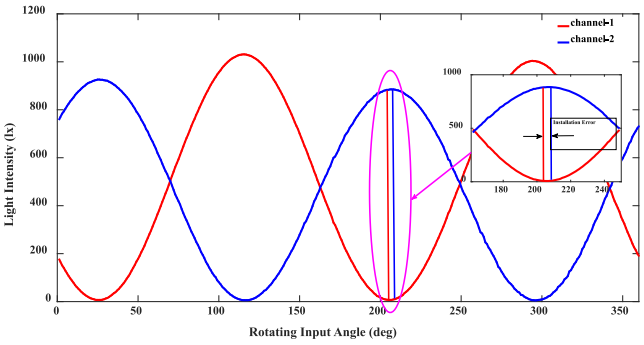

FIGURE 2. The raw light intensity outputs of channel-1 and channel-2.

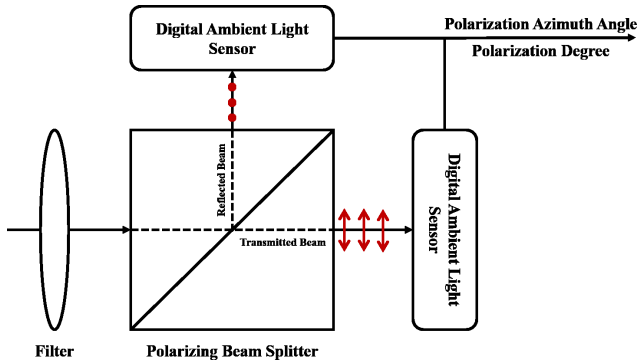

FIGURE 3. The polarization beam splitter sketch map.

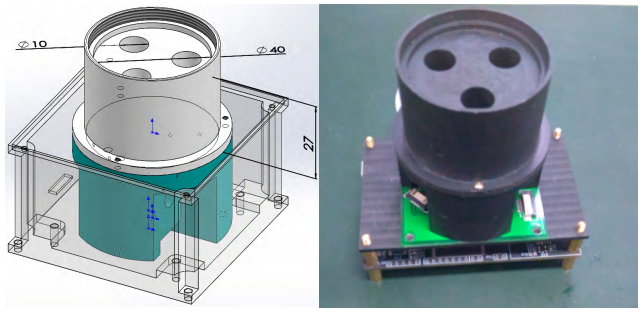

FIGURE 4. The physical diagram of the sensor.

In this paper, we use a PBS as the sensor analyzer to eliminate the quadrature error. The PBS can divide the natural light into two beams of mutually orthogonal polarized light, as shown in Fig. 3. In the sensor design, we choose the PBS101 from Thorlabs as the PBS, which is 10 mm × 10 mm × 10 mm in size. The coating range of PBS101 is from 420nm to 680nm which can receive polarized skylight in the blue band. The transmitted beam extinction ratio is greater than 1000:1, but the reflected one is much smaller, from 20:1 to 100:1. The difference of the extinction ratio consistency between the two beams directly affects the sensor accuracy and stability. Thus, this factor should to be considered in sensor modeling, which will be detailed in Section III.

In addition, the optoelectronic device we choose is the BH1750FVI from Rohm. The BH1750FVI is a digital ambient light sensor of 16-bit serial output type and can detect a wide range of light at high resolution (1lx-65535lx). In the sensor design, we have considered the oblique light and stray light effect on polarization optical acquisition. To ensure the incident light is irradiated perpendicularly to the PBS, that is the angle of incidence is 90°, a drawtube is designed in this paper. The sensor physical diagram is shown in Fig.4.

The drawtube is a lens hood, which can avoid the effect of external oblique stray light on the PBS. The drawtube diameter is 40 mm, and there are three light apertures which are around the drawtube center. To ensure the consistency of the incident light intensity, the three light apertures are designed into a symmetrical structure. After plenty of validation, the light aperture diameter is designed as 10mm and the length is 27mm, as shown in Fig.4. By this design, the sunlight passes through the light aperture and the incident light is irradiated vertically on the PBS. What's more, the internal face of the light aperture is black which is used to absorb the light slanted. This design can also effectively reduce the influence of incidence angle on polarization optical information acquisition.

The sensor obtains photoelectric signals from the output of three units and calculates the polarization azimuth angle in real time, which is then transmitted to the host computer through a serial port. The sensor designed in this paper is 5.5 cm × 5.5 cm × 6.5 cm in size and 50 g in weight, which can meet the requirement of UAV applications.

III. SENSOR MODELING AND POLARIZATION ALGORITHM

In Section II, we have known that the PBS can polarize the incident non-polarized light into two orthogonal polarized beams. However, the transmitted polarized light (TPL) will enter the path of the reflected polarized light (RPL) one and vice versa. The mutual coupling of the two beams directly affects the measurement accuracy and stability of the sensor. Furthermore, the transmitted beam extinction ratio is greater than the reflected one. The extinction ratio inconsistency between the two beams also influences the sensor performance.

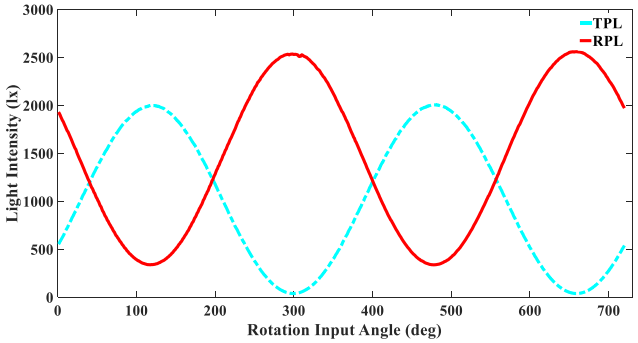

FIGURE 5. The raw light intensity output of TPL and RPL.

In Section III, to solve the problems mentioned above, we establish a sensor model, where we introduced a coupling coefficient to suppress the coupling interference and extinction ratio inconsistency between the two beams polarized light. And then an independent-channel algorithm is presented to calculate the polarization degree (PD) and the polarization azimuth angle (PA) based on the proposed model.

A. SENSOR MODELING

Ideally, the TPL and the RPL have the same amplitude and opposite phase. However, due to the coupling of the two optical signals, the light intensity is not consistent. In practice, the TPL will enter the path of the RPL one and vice versa. The raw data of light intensity is obtained under the laboratory standard light environment, as shown in Fig.5. The result shows that the TPL and RPL coexist in one channel at the same time. Accordingly, the TPL and RPL are partially polarized and the two beams are presented a mixed state of polarization.

Suppose both the two beams are fully polarized light, the outputs of TPL and RPL can be expressed as follows [13]:

$$\begin{aligned} I_t &= K_t I_{in}(1 + d\cos 2(\varphi + \alpha)) \\ I_r &= K_r I_{in}(1 - d\cos 2(\varphi + \alpha)) \end{aligned} \tag{1}$$

where I_t and I_r are the output light intensities of TPL and RPL, K_t and K_r are the light intensity coefficients of TPL and RPL, respectively, I_{in} is the incident light intensity, d denotes the polarization degree, φ is polarization azimuth angle, α is the angle between the analyzer orientation and the zero-position direction of the sensor.

According to the characteristics of PBS, the transmitted beam and the reflected beam are orthogonal polarized light, and the output of one beam can be expressed as the combination of the two beams [32], as seen in Equation (2)

$$I_{out} = K_t I_{in}(1 + d\cos 2(\varphi + \alpha)) + K_r I_{in}(1 - d\cos 2(\varphi + \alpha)) \tag{2}$$

We set

$$K_I = K_t + K_r, K_d = (K_t - K_r)/(K_t + K_r) \tag{3}$$

Then, Equation (2) can be simplified as

$$I_{out} = K_I I_{in}(1 + K_d d\cos 2(\varphi + \alpha)) \tag{4}$$

Thus, the novel sensor model based on PBS is given by Equation (4). The K_I is the light intensity coefficient which characterize the light intensity gains and losses of the whole optical path. Compared with the existing sensor models [12], [17], a newly introduced coupling coefficient K_d is proposed, which characterized the extinction ratio performance of the sensor.

Importantly, this coefficient has great influence on sensors with low extinction ratio or poor consistency in extinction ratio. As we have mentioned in Section II, the extinction ratio between the TPL and RPL are quite different. If the K_d is uncalibrated, the PD and PA will show large-scale fluctuations, which will be detailed in Section IV. In what follows, we will carry out calibration experiments and adopt the UKF method to identify these parameters.

B. POLARIZATION ALGORITHM

As we have presented in subsection A, a coefficient K_d is introduced to the sensor model. Consequently, we need to calculate the PD and PA based on the sensor model proposed in this paper. According to the prismatic specialty of the PBS, the channels of the TPL and RPL are treated as two independent detection units.

The sensor consisting of three PBS can acquire six channel light intensity measurements simultaneously. Supposing that the sensor measurement error be v, the six channel outputs can be expressed as follows

$$I_i = K_{I_i} I_{in}\left(1 + K_{d_i} d\cos 2\left(\varphi + \alpha_i\right)\right) + v_i i = 1, \cdots, 6 \tag{5}$$

where I_i, K_{I_i}, K_{d_i} and α_i are the output light intensity, light intensity coefficient, coupling coefficient, and polarization detection angle of the i-th channel.

By the cosine formula, Equation (5) can be transformed into

$$\begin{aligned} I_i = K_{I_i} I_{IN} + K_{I_i} K_{d_i} I_{IN} d\cos 2\varphi \cos 2\alpha_i \\ - K_{I_i} K_{d_i} I_{IN} d\sin 2\varphi \sin 2\alpha_i + v_i \end{aligned} \tag{6}$$

Then the six channel measurements can be written in matrix form:

$$y = Hx + v \tag{7}$$

where

$$\begin{aligned} x &= [\,x(1)\ x(2)\ x(3)\,]^T = \left[\,I_{in}\ I_{in}d\cos 2\varphi\ I_{in}d\sin 2\varphi\,\right]^T \\ y &= [I_i]_{6\times 1} \\ H &= \left[\,K_{I_i}\ K_{I_i}K_{d_i}\cos 2\alpha_i\ -K_{I_i}K_{d_i}\sin 2\alpha_i\,\right]_{6\times 3} \\ v &= [v_i]_{6\times 1} \end{aligned}$$

The least-squared estimation of x is expressed as follows:

$$\hat{x} = \left(H^T H\right)^{-1} H^T y \tag{8}$$

Once the $\hat{x}$ is obtained, the PD and PA can be solved by

$$\begin{aligned}\hat{d} &= \sqrt{\hat{x}\,(2)^2 + \hat{x}\,(3)^2}/\hat{x}\,(1)\\ \hat{\varphi} &= 0.5\arctan\left(\hat{x}\,(2)/\hat{x}\,(3)\right)\end{aligned} \tag{9}$$

where $\hat{x}\,(1)$, $\hat{x}\,(2)$, and $\hat{x}\,(3)$ are the estimated values of $x(1)$, $x(2)$, and $x(3)$, respectively.

IV. SENSOR CALIBRATION

According to the polarization algorithm presented in Section III, we have known that each PBS has five parameters to be identified: K_I, K_d, d, φ, and α. In this section, the UKF method [28], [29] is adopted to estimate these five parameters. The calibration process mainly includes three steps: the first step is to determine the initial values of these parameters and the second step is to build the sensor state equation and measurement equation. The third step is to use the UKF to identify the parameters.

A. PARAMETER INITIAL VALUE DETERMINE

In the indoor environment, the standard polarized light is generated by one integrating sphere and a linear polarizer. During the test, the sensor is sampled uniformly in N directions, the polarization azimuth angle at the n-th sampling point is given by

$$\varphi_n = \varphi_0 + 2\pi n/N \quad n = 0, 1, \ldots, N-1 \tag{10}$$

According the trigonometric function, we have

$$\begin{aligned}&\sum_{n=0}^{N-1}\sin 2\varphi_n = \sum_{n=0}^{N-1}\cos 2\varphi_n = \sum_{n=0}^{N-1}\sin 2\varphi_n\cos 2\varphi_n = 0\\ &\sum_{n=0}^{N-1}\sin^2 2\varphi_n = \sum_{n=0}^{N-1}\cos^2 2\varphi_n = \frac{N}{2}\end{aligned} \tag{11}$$

If the measurement error is not considered, the output light intensity of the n-th sample is shown in Equation (12):

$$I_i\,(n) = K_{I_i} I_{in}\left(1 + K_{d_i} d\cos 2\left(\varphi_i(n) + \alpha_i\right)\right) \tag{12}$$

Combining Equation (12) with Equation (11), we have

$$\begin{aligned}K_{I_i} &= \frac{1}{N}\sum_{n=0}^{N-1} I_i\,(n)/I_{IN}\\ K_{d_i} &= \left(N\sqrt{\frac{2}{N}\sum_{n=0}^{N-1}\left(I_i\,(n) - K_{I_i} I_{in}\right)^2}\right)\Big/\left(d\sum_{n=0}^{N-1} I_i\,(n)\right)\\ \alpha_i &= 0.5\arctan\left(\sum_{n=0}^{N-1} I_i\,(n)\cos 2\varphi_n \Big/ \sum_{n=0}^{N-1} I_i\,(n)\sin 2\varphi_n\right)\end{aligned} \tag{13}$$

Then, Equation (12) can be expressed in the matrix form

$$y_n = H_n x_n \tag{14}$$

where

$$\begin{aligned}y_n &= [I_i\,(n)]_{6\times N}\\ x_n &= \left[\, I_{in} \;\; I_{in} d\cos 2\varphi_i(n) \;\; I_{in} d\sin 2\varphi_i(n)\,\right]_{3\times N}\\ H_n &= \left[\, K_{I_i} \;\; K_{I_i} K_{d_i}\cos 2\alpha_i \;\; -K_{I_i} K_{d_i}\sin 2\alpha_i\,\right]_{6\times 3}\end{aligned}$$

Then we get the least-squared estimation of H_n, as shown in Equation (15)

$$\hat{H}_n^T = y_n\left(x_n^T x_n\right)^{-1} x_n^T \tag{15}$$

Once the is $\hat{H}_n^T$ obtained, the coefficients K_{I_i}, K_{d_i}, and α_i can be expressed as follows

$$\begin{aligned}K_{I_i} &= \hat{H}_n^T\,(i, 1)\\ K_{d_i} &= \sqrt{\hat{H}_n^T\,(i, 2)^2 + \hat{H}_n^T\,(i, 3)^2}/\hat{H}_n^T\,(i, 1)\\ \alpha_i &= 0.5\arctan\left(\hat{H}_n^T\,(i, 2)/\hat{H}_n^T\,(i, 3)\right)\end{aligned} \tag{16}$$

where $\hat{H}_n^T\,(i, 1)$, $\hat{H}_n^T\,(i, 2)$, and $\hat{H}_n^T\,(i, 3)$ are the first, second and third column of $\hat{H}_n^T$.

Based on Equation (13) and (16), the initial parameter values can be determined. The next step is to establish the sensor state equation and measurement equation.

B. STATE AND MEASUREMNT EQUATION

The second step is to establish the sensor state equation and measurement equation. The sensor state equation is a 18-dimensional vector which contains K_I, K_d, α of each channel and the d, and φ, given by

$$r = [K_{I_1}\cdots K_{I_6} K_{d_1}\cdots K_{d_6}\alpha_1\cdots\alpha_6 d\varphi]^T \tag{17}$$

Then, the state equation can be expressed as follows

$$r_{k+1} = r_k + u_k + w_k = f\,(r_k, u_k) + w_k \tag{18}$$

where f is the sensor state matrix, w_k is the process noise, u_k is the control input which is given by

$$u_k = [0_{1\times 17}\Delta\varphi_{u_k}]^T \tag{19}$$

where $\Delta\varphi_{u_k}$ is the angle variation of electric turntable.

The sensor measurement vector is comprised of six channels of output light intensity, the polarization degree of light source d_k, and the rotation angle φ_k of the electric turntable. The sensor measurement equation is expressed as

$$z_k = [I_1(k)\cdots I_6(k) d_k\sin(\varphi_k)]^T \tag{20}$$

According to Equation (12), the measurement equation is given by

$$\begin{aligned}z_k &= h\,(r_k, \omega_k)\\ &= \begin{bmatrix} K_{I_1} I_{in}\left(1 + K_{d_1} d\cos 2\left(\varphi_k + \alpha_1\right)\right) + \omega_1\\ K_{I_2} I_{in}\left(1 + K_{d_2} d\cos 2\left(\varphi_k + \alpha_2\right)\right) + \omega_2\\ K_{I_3} I_{in}\left(1 + K_{d_3} d\cos 2\left(\varphi_k + \alpha_3\right)\right) + \omega_3\\ K_{I_4} I_{in}\left(1 + K_{d_4} d\cos 2\left(\varphi_k + \alpha_4\right)\right) + \omega_4\\ K_{I_5} I_{in}\left(1 + K_{d_5} d\cos 2\left(\varphi_k + \alpha_5\right)\right) + \omega_5\\ K_{I_6} I_{in}\left(1 + K_{d_6} d\cos 2\left(\varphi_k + \alpha_6\right)\right) + \omega_6\\ d_k + \omega_7\\ \sin(\varphi_k + \omega_8)\end{bmatrix}\end{aligned} \tag{21}$$

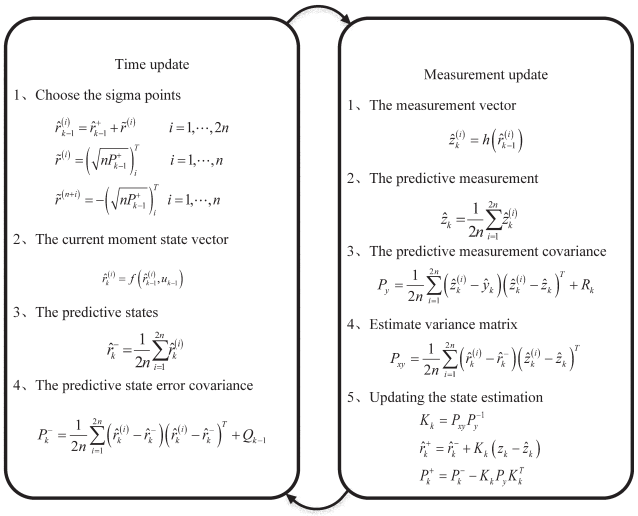

FIGURE 6. UKF algorithm flow chart.

where h is the sensor measurement matrix, and ω_k is the measurement noise.

C. UKF CALIBRATION

After establishing the sensor state equation and measurement equation, our next job is to identify these parameters. From Equation (21), we can see that the measurement equation is a nonlinear model. In this part, we adopt the UKF to identify the parameters. The calibration procedure is shown in Fig.6 [29].

Combined with the sensor initial estimated parameters values obtained in the first step, the measured data is filtered iteratively to make the state estimation stable. In the calibration process, we take the median value of the steady-state process as the final parameter estimation.

V. CALIBRATION EXPERIMENTS

In this section, indoor calibration and outdoor fixed-point static experiments are carried out. The purpose of the indoor calibration experiment is to verify the proposed sensor model under a standard environment. In the outdoor sky conditions, however, the environmental factors, such as cloud cover, large particles in clouds, aerosols, water and wet soil surfaces, rocks, etc. [30], [31], will directly influence the performance of the sensor. To test the stability performance of the sensor, an outdoor fixed-point accuracy experiment is also carried out in this section.

A. INDOOR CALIBRATION EXPERIMENT

The indoor calibration equipment is shown in Fig.7 (a). The equipment mainly includes an integrating sphere, a linear polarizer, an optical platform and a high precision electric turntable, etc. The integrating sphere and the linear polarizer with high extinction ratio (9000:1) is used to generate the standard polarized light in the lab environment. In the experiment, the variation of the turntable rotation angle is used as

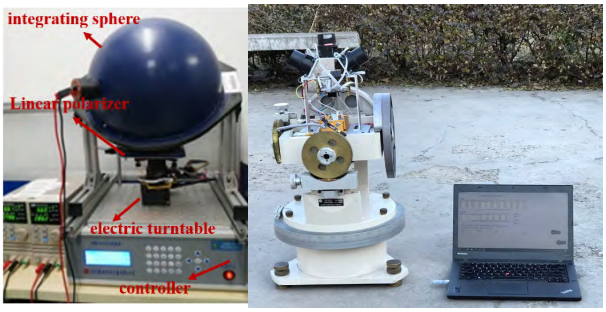

FIGURE 7. Testing equipment. (a). The indoor calibration equipment. (b). The outdoor calibration and long-term fixed-point test equipment.

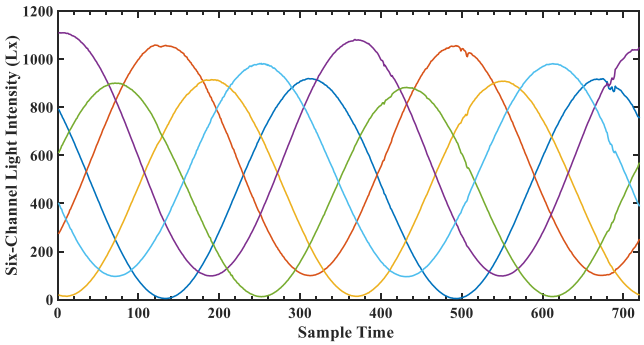

FIGURE 8. Six channels light intensity output curves.

the calibration reference of the polarization azimuth angle. The optical platform is used to provide a stable horizontal reference plane for the experiment, ensuring that the optical axis of sensor is aligned with the light outlet of the integrating sphere.

During the indoor calibration experiment, to avoid the interference of external stray light, the experiment was constructed in a dark room. The light generated by integrating sphere and linear polarizer was taken as a completely linearly polarized light, that the degree of polarization is 1. The electric turntable rotated discretely once 0.5° and the six channels' raw light intensity values were sampled during the process, as shown in Fig.8. In the experiment, the electric turntable turned 360° and collected 720 samples in total.

As we have mentioned in Section II and Section III, the optical path coupling problem and the difference of extinction ratio consistency between the two beams directly affects the sensor accuracy and stability. The initial light intensity response curves also confirm the problems discussed above. In Fig. 8, we can see that the light intensity of each channel still evolves in a sinusoidal or cosine manner, but the light amplitudes of each channel are different from each other. To verify the new sensor model proposed in this paper, we process the raw data obtained from the experiments under three cases:

Case 1: parameters un-calibrated;
Case 2: parameters partially calibrated (K_I and α);
Case 3: parameters fully calibrated (K_I, K_d, and α).

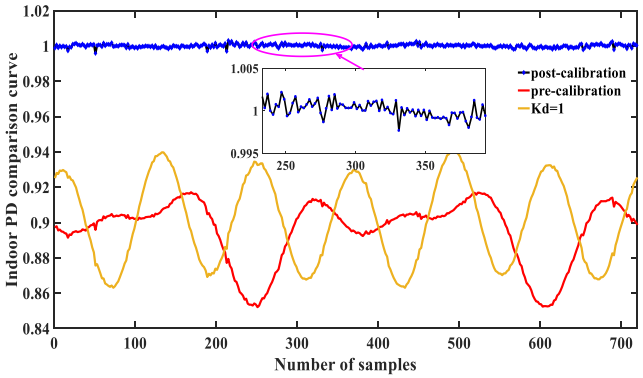

FIGURE 9. Indoor polarization degree measurement curves.

TABLE 1. Sensor indoor calibration parameters.

	Chan 1	Chan 2	Chan 3	Chan 4	Chan 5	Chan 6
Case 1	1.0000	1.2591	1.0044	1.2796	0.9750	1.1653
Case 2	0.9896	0.8264	0.9705	0.8325	0.9720	0.8214
Case 3	0.0000	89.6117	-61.632	28.1797	59.5877	-31.799

TABLE 2. Indoor experiment pd calibration results.

PD (%)	Mean Absolute Error	Mean Square Error	Maximum Error
Case 1	0.1479	0.0240	-0.0828
Case 2	0.1370	0.0179	-0.0597
Case 3	0.0041	9.5419e-04	0.0031

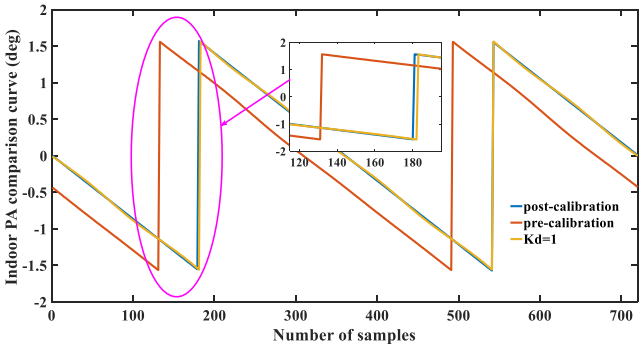

FIGURE 10. Indoor polarization azimuth angle measurement curves.

Note that the purpose of Case 2 is to verify the influence of the newly introduced coupling coefficient on the sensor model. In this case, the coefficients K_I and α are calibrated, the coefficients K_d is not taken into consideration.

Fig. 9 shows different PD measurement outputs in the three cases. The red curve represents the PD output in Case 1, the orange one represents the PD output in Case 2, and the blue one represents the PD output in Case 3, respectively. In Case 1, we can see that the PD measurement exhibits irregular large-scale fluctuations without calibration, and the PD measurement standard deviation error before calibration is 0.0240 (1σ) and the maximum error is up to -0.0828.

In Case 2, the K_d is not taken into consideration as same as Case 1, the sensor model of which can be simplified as Equation (1). From Fig. 9 we can see that, compared with Case 1, the PD measurement result (the orange curve) in Case 2 also exhibits large-scale fluctuations without consideration of K_d. However, the PD output curve in Case 2 is more regular. This difference between the two curves is mainly caused by K_I and α. Note that the large-scale fluctuations in Case 2 is resulted of the optical coupling and extinction ratio inconsistency between the TPL and RPL. In Case 2, the PD measurement standard deviation error is 0.0179 (1σ), and the maximum error is -0.0597. Compared with Case 1, the PD measurement accuracy has been improved by 1.3408 times.

In Case 3, we consider that the K_d is not equal to 1. In this case, we adopted the UKF to calibrate the three parameters. The calibrated parameters are shown in Table 1. In Fig. 9, compared with the PD output curves of Case 1 and Case 2, we can see that Case 3 (the blue curve) after parameters fully calibrated is smoother and showing smaller fluctuations, see the partial enlarged view of the blue curve. In Case 3, the PD measurement standard deviation error is 9.5419e-04 (1σ), and the maximum error is not exceeded 0.0031. Compared with Case 2, the accuracy has been increased by 18.7593 times. The K_d effectively suppresses the interaction between the transmitted beam and the reflected beam. The indoor calibration results of PD are presented in Table 2.

In addition, the PD measured value is close to the value generated by the integrating sphere and the linear polarizer. In comparison of the results under the three cases, we can conclude that an enhanced performance is achieved by the parameters fully calibrated process. On the other hand, our results also verified the sensor model proposed in Section II. The new introduced coefficient K_d can effectively reduce the influence of the extinction ratio inconsistency on the sensor accuracy and stability.

The PA measurements results are shown in Fig. 10. The blue curve, the yellow curve and the red one denote the PA results in the three cases, respectively. As can be seen from the results, there is a 0.4365° constant deviation between the pre-calibration and post-calibration results. This deviation is mainly caused by α, and can be compensated after α is calibrated, as seen from the partial enlargement from the 115^{th}-195^{th} sampling points.

Fig. 11 presents the PA error comparison curve. In the experiment, we chose the angle change amount of electric turntable rotation as the reference. In Case 1 (the red curve), the maximum error of PA is 0.4096° and the standard deviation is 0.0134° (1σ). After K_I and α are calibrated, it is obvious that the error curve (the orange one) is more stable in Case 2. The PA maximum measurement error is 0.0224° and the standard deviation is 0.0122° (1σ). The blue curve (Case 3) is the PA measurement error results after the parameter fully calibrated. From the comparison results, we can see that the PA precision has a significant improvement when is K_d calibrated and the PA measurement maximum error is not exceeded 0.0030°. Through the introduced K_d, the accuracy

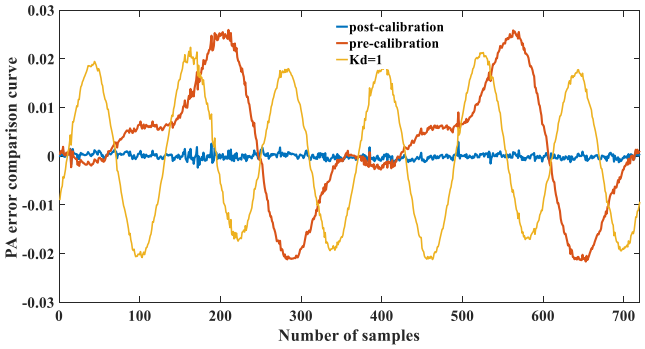

FIGURE 11. Indoor polarization azimuth angle error curves.

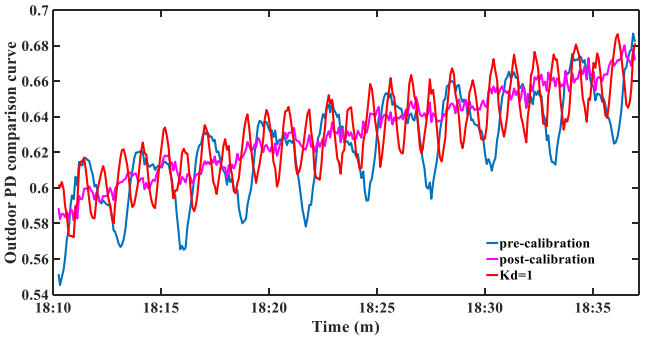

FIGURE 12. Outdoor polarization degree comparison curves.

TABLE 3. Indoor experiment pa error comparison.

PA (°)	Mean Absolute Error	Mean Square Error	Maximum Error
Case 1	0.4334	0.0134	-0.4096
Case 2	0.0121	0.0122	0.0224
Case 3	0.0004	0.0006	0.0030

TABLE 4. Sensor indoor calibration parameters.

	Chan 1	Chan 2	Chan 3	Chan 4	Chan 5	Chan 6
Case 1	1.0023	1.3560	1.0262	1.3458	0.9952	1.3198
Case 2	1.0222	0.7922	1.0016	0.8185	1.0050	0.8364
Case 3	0.0000	89.4991	-60.769	29.2916	60.3020	-30.534

of PA has been increased by 20.2336 times. The PA error precision comparison among the three cases is shown in Table 3.

B. OUTDOOR STATIC ACCURACY EXPERIMENT

In the indoor calibration experiment, we have already verified the sensor model and discussed the influence of K_d on sensor accuracy. However, when the polarization sensor is applied in the outdoor conditions, the external disturbances, such as the direct sunlight, the spectrum of the solar, etc., will directly affect the optical device performance. In this subsection, we will test the sensor static accuracy in the sky conditions.

The outdoor static accuracy experiment equipment is shown in Fig. 7 (b). The polarization sensor was placed on a non-magnetic turntable guaranteed the sensor keep level during the outdoor static accuracy test. What's more, the turntable can be the reference for the polarization azimuth angle. A wireless transmission module is designed to facilitate the transmission and storage of sensor data.

The outdoor static accuracy experiment was constructed in the garden of liberal arts school (116°20 ′N, 39°58 ′E), BUAA, Beijing, China. The experiment time was Beijing time 18: 09 on Sept. 2nd, 2016, under sunny condition. To reduce the effects of direct sunlight and other external factors, the experiment was carried out at nightfall to ensure a better d-pattern of skylight at the zenith point. In the outdoor long-term static accuracy experiment, we also considered the same three cases as the indoor calibration procedure:

Case 1: parameter uncalibrated;

Case 2: parameter partial calibrated;

Case 3: parameter fully calibrated.

During the tests, we kept the turntable in a horizontal state to ensure that the sensor was always facing the zenith direction. The turntable was rotated once every 5°, and the sensor output was recorded as an individual sample. After consecutive sampling for a period of time, we got three PD measurement curves in Fig. 12.

Be similar with the indoor calibration experiment, there are three sets experiment results. From Fig. 12, we can observe that the PD output curves shows large-scale fluctuations in Case 1 (the blue curve) and Case 2 (the red curve). In Case 3, after the K_d has been calibrated, the PD output curve (the pink one) also exhibit fluctuations, which is resulted in the changes of sky conditions. However, compared with the other two curves, the pink one is more stable. From Fig. 12, we can see that, with the increase of time, the PD increases accordingly. The reason for this phenomenon is that with the decrease of solar elevation angle during the experiment time, the scattering angle between the observed point and the solar vector is increased. According to the Rayleigh Scattering Theory, the PD measurement value is also increased accordingly. The results of the calibrated parameters are shown in Table 4.

Compared with the parameter calibrated results in the indoor ideal environment, the coefficient K_I and α vary slightly. The amplitude of variation of K_I changes from 1.71% to 4.14% and the α changes from 0.13% to 4.14%. On the other hand, the K_I is influenced by solar spectral component and light intensity, compared with the indoor calibrated parameters, the maximum amount of variation of is up to 11.71%.

Fig. 13 shows the PA measurement error comparison curves. We chose the angle change amount of the turntable as reference. The blue curve is the PA measurement result in Case 1. From the figure, we can see that the PA maximum measurement error is up to 2.52° and the standard deviation is 1.01° (1σ). In Case 2 (the red curve), the PA maximum measurement error is 1.39° and the standard deviation is reduced to about 0.66° (1σ). Compared with Case 1, the PA measurement accuracy has been increased by 1.5367 times. The pink

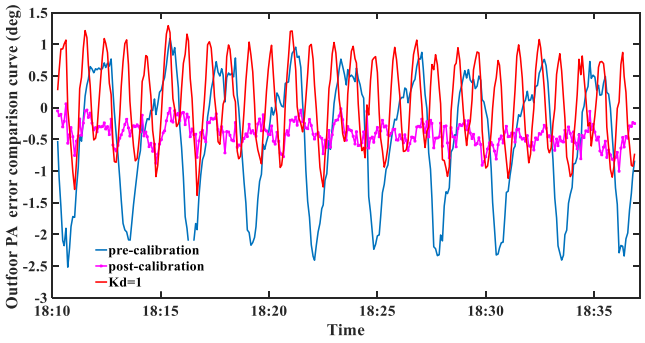

FIGURE 13. Outdoor polarization azimuth angle error curves.

TABLE 5. Outdoor experiment pa error results.

PA error (°)	Mean Absolute Error	Mean Square Error	Maximum Error
Case 1	0.88	1.01	2.52
Case 2	0.58	0.66	1.38
Case 3	0.42	0.18	1.00

curve donates the PA measurement results in Case3. As can be seen from the result, the PA maximum measurement error is not exceeded 1.00° and the standard deviation achieves 0.18° (1σ), as seen in Table 5. Form the outdoor PA measurement error comparison results, we can see that the PA accuracy has a marked improvement in Case 3. Compared with Case 2, the accuracy has been increased by 3.5836 times. The outdoor experiments error results of PA are shown in Table 5. The outdoor static experiment shows that the sensor designed in this paper has higher precision and can maintain a long-time stability.

VI. CONCLUSION

In this paper, we designed a new bionic polarization navigation sensor based on polarizing beam splitter, by imitating the polarization structure of insects' compound eyes. The splitter can effectively reduce the quadrature error caused by the polarization detection device of the sensor. According to the new structure of the sensor, the novel sensor model was established. Different from the existing models, a new coefficient K_d was introduced in the sensor model. The not only can characterize the extinction ratio performance of the sensor, but also resolve the coupling problem between the TPL and RPL. We also proposed an independent-channel polarization calculation method and adopted the UKF calibration method to identify the sensor parameters. A mount of indoor and outdoor calibration experiments was conducted, respectively. The calibration results confirmed the validity of the established model and the effectiveness of the proposed algorithm. Furthermore, a long-term stability test was also carried out with satisfactory results, achieving an accuracy of 0.18°. Future work long this line of research includes the sensor error analysis, calibration and compensations. The application of polarization navigation sensor in UAVs is also a very relevant topic in future research.

REFERENCES

[1] R. Wehner, "Desert ant navigation: How miniature brains solve complex tasks," *J. Comparative Phys. A*, vol. 189, no. 8, pp. 579–588, 2003.
[2] S. Greif, I. Borissov, Y. Yovel, and R. A. Holland, "A functional role of the sky's polarization pattern for orientation in the greater mouse-eared bat," *Nature Commun.*, vol. 5, no. 3, May 2014, Art. no. 4488.
[3] J. L. Gould, "Sensory bases of navigation," *Current Biol.*, vol. 8, no. 20, pp. R731–R738, 1998.
[4] J. Chahl and A. Mizutani, "Biomimetic attitude and orientation sensors," *IEEE Sensors J.*, vol. 12, no. 2, pp. 289–297, Feb. 2012.
[5] M. Hamaoui, "Polarized skylight navigation," *Appl. Opt.*, vol. 56, no. 3, pp. B37–B46, 2017.
[6] R. Jianbin, L. Jun, T. Jun, W. Chenguang, and X. Chenyang, "Attitude determination based on location of astronomical markers with skylight polarization pattern," *IEEE Sensors J.*, vol. 15, no. 12, pp. 7312–7320, Dec. 2015.
[7] T. Labhart and E. P. Meyer, "Neural mechanisms in insect navigation: Polarization compass and odometer," *Current Opinion Neurobiol.*, vol. 12, no. 6, pp. 707–714, 2002.
[8] G. Horváth, *Polarized Light and Polarization Vision in Animal Sciences*. Berlin, Germany: Springer, Feb. 2014.
[9] H. Lu, K. Zhao, Z. You, and K. Huang, "Real-time polarization imaging algorithm for camera-based polarization navigation sensors," *Appl. Opt.*, vol. 56, no. 11, pp. 3199–3205, 2017.
[10] J. K. Chu, Z. Wang, L. Guan, Z. Liu, Y. Wang, and R. Zhang, "Integrated polarization dependent photodetector and its application for polarization navigation," *IEEE Photon. Technol. Lett.*, vol. 26, no. 5, pp. 469–472, Mar. 1, 2014.
[11] D. Wang, H. Liang, H. Zhu, and S. Zhang, "A bionic camera-based polarization navigation sensor," *Sensors*, vol. 14, no. 7, pp. 13006–13023, 2014.
[12] Z. Xian *et al.*, "A novel angle computation and calibration algorithm of bio-inspired sky-light polarization navigation sensor," *Sensors*, vol. 14, no. 9, pp. 17068–17088, 2014.
[13] S. B. Karman, S. Zaleha M. Diah, and I. C. Gebeshuber, "Bio-inspired polarized skylight-based navigation sensors: A review," *Sensors*, vol. 12, no. 11, pp. 14232–14261, 2012.
[14] D. Lambrinos, H. Kobayashi, R. Pfeifer, M. Maris, T. Labhart, and R. Wehner, "An autonomous agent navigating with a polarized light compass," *Adapt. Behav.*, vol. 6, pp. 131–161, Jun. 1997.
[15] D. Lambrinos, R. Moller, T. Labhart, R. Pfeifer, and R. Wehner, "A mobile robot employing insect strategies for navigation," *Robot. Auto. Syst.*, vol. 30, pp. 39–64, Jan. 2000.
[16] J. Chu, K. Zhao, Q. Zhang, and T. Wang, "Construction and performance test of a novel polarization sensor for navigation," *Sens. Actuators A, Phys.*, vol. 148, no. 1, pp. 75–82, 2008.
[17] K. Zhao, J. Chu, T. Wang, and Q. Zhang, "A novel angle algorithm of polarization sensor for navigation," *IEEE Trans. Instrum. Meas.*, vol. 58, no. 8, pp. 2791–2796, Aug. 2009.
[18] L. Jianjun, D. Tao, Y. Jian, Z. Qian, and G. Lei, "Research on a method of polarization azimuth calculation with photoelectric sensor," in *Proc. IEEE 33rd Chin. Control Conf. (CCC)*, Jul. 2014, pp. 936–941.
[19] T. Ma, X. Hu, L. Zhang, and X. He, "Calibration of a polarization navigation sensor using the NSGA-II algorithm," *Opt. Commun.*, vol. 376, no. 1, pp. 107–114, 2016.
[20] T. Ma, X. Hu, J. Lian, and L. Zhang, "A novel calibration model of polarization navigation sensor," *IEEE Sensors J.*, vol. 15, no. 8, pp. 4241–4248, Aug. 2015.
[21] R. Zhang, J. Chu, Z. Liu, and Y. Wang, "Simple integration process of single-layer nanowire gratings for polarization navigation sensor," *J. Micro/Nanolithogr., MEMS, MOEMS*, vol. 15, no. 3, p. 034501, 2016.
[22] Z. Wang, J. Chu, Q. Wang, and R. Zhang, "Single-layer nanowire polarizer integrated with photodetector and its application for polarization navigation," *IEEE Sensors J.*, vol. 16, no. 17, pp. 6579–6585, Sep. 2016.
[23] M. Sarkar, D. S. S. Bello, C. van Hoof, and A. Theuwissen, "Biologically inspired autonomous agent navigation using an integrated polarization analyzing CMOS image sensor," *Procedia Eng.*, vol. 5, no. 3, pp. 673–676, 2010.
[24] M. Sarkar, D. S. S. Bello, C. van Hoof, and A. Theuwissen, "Integrated polarization analyzing CMOS Image sensor for autonomous navigation using polarized light," in *Proc. 5th IEEE Int. Conf. Intell. Syst. (IS)*, Jul. 2010, pp. 224–229.

[25] C. Fan, X. Hu, J. Lian, L. Zhang, and X. He, "Design and calibration of a novel camera-based bio-inspired polarization navigation sensor," *IEEE Sensors J.*, vol. 16, no. 10, pp. 3640–3648, May 2016.
[26] Y. Wang, X. Hu, J. Lian, L. Zhang, and X. He, "Bionic orientation and visual enhancement with a novel polarization camera," *IEEE Sensors J.*, vol. 17, no. 5, pp. 1316–1324, Mar. 2017.
[27] T. Labhart and E. P. Meyer, "Detectors for polarized skylight in insects: A survey of ommatidial specializations in the dorsal rim area of the compound eye," *Microscopy Res. Techn.*, vol. 47, no. 6, pp. 368–379, 1999.
[28] L. Guo, S. Cao, C. Qi, X. Gao, "Initial alignment for nonlinear inertial navigation systems with multiple disturbances based on enhanced anti-disturbance filtering," *Int. J. Control*, vol. 85, no. 5, pp. 491–501, 2012.
[29] D. Simon, *Optimal State Estimation: Kalman, H Infinity, and Nonlinear Approaches*. Hoboken, NJ, USA: Wiley, 2006, pp. 448–451.
[30] R. Hegedüs, S. Åkesson, and G. Horváth, "Polarization patterns of thick clouds: Overcast skies have distribution of the angle of polarization similar to that of clear skies," *J. Opt. Soc. Amer. A, Opt. Image Sci.*, vol. 24, no. 8, pp. 2347–2356, 2007.
[31] K. L. Coulson, *Polarization and Intensity of Light in the Atmosphere*, 1st ed. Hampton, VA, USA: Deepak, 1988.
[32] R. Shintani, A. Fan, and C. Kang, *Polarized Light*. Beijing, China: Atomic Energy Press, 1994, p. 52.

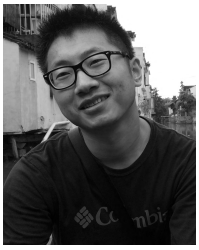

JIAN YANG was born in Chifeng, China, in 1987. He received the B.S. degree from the Department of Automatic Control, Northeastern University, Shenyang, China, in 2011. He is currently pursuing the Ph.D. degree with Beihang University, Beijing, China. His current research interests include bionic polarization navigation, autonomous navigation systems, and filter design with their applications to aerospace systems.

TAO DU received the Ph.D. degree in control theory and control engineering from the School of Automation, Southeast University, Nanjing, China, in 2016. He is currently a Lecturer with the School of Electronics and Information Engineering, North China University of Technology. His current research interests include inertial-based integrated navigation systems and state estimation theory.

BEN NIU was born in Jiyuan, China, in 1986. He received the B.S. degree from the School of Automation, Nanjing University of Science and Technology, Nanjing, China, in 2008, and the M.S. degree in control theory and control engineering from the School of Automation Science and Electrical Engineering, Beihang University, Beijing, China, in 2017. His current research interests are bionic polarization sensor calibration and outdoor test.

CHENYANG LI was born in Weihai, China, in 1991. He received the B.Sc. degree from the School of Automation, Beijing University of Technology, Beijing, China, in 2013, and the M.S. degree in control theory and control engineering from the School of Automation Science and Electrical Engineering, Beihang University, Beijing, in 2017. His current research interests are bionic polarization sensor design and calibration compensation method.

JIANQIANG QIAN received the Ph.D. degree in precision instrument from Tsinghua University in 2005. He is currently a Professor with the School of Physics and Nuclear Energy Engineering, Beihang University, where he is also the Deputy Director of the Department of Applied Physics. He is a member of the Key Laboratory of Micro-nano Measurement-Manipulation and Physics, Ministry of Education, China. His research focuses on the application of automatic and intelligent control theory to micronano measurement and manipulation.

LEI GUO was born in Qufu, China, in 1966. He received the B.S. and M.S. degrees from Qufu Normal University, Qufu, in 1988 and 1991, respectively, and the Ph.D. degree in control engineering from Southeast University, Nanjing, China, in 1997. He has authored or co-authored over 120 papers and one monograph. His research interests include robust control, stochastic systems, fault detection, filter design, and nonlinear control with their applications to aerospace systems. He received the National Science Fund for Distinguished Young Scholars of China and a Changjiang Distinguished Professorship from the Ministry of Education of China. He served as an Editor for five journals.